

Nanodosimetric characterisation of proton track structure: a comparison of sampling and clustering algorithms using Geant4-DNA

João F. Canhoto^{1,2,*}, Yann Perrot³, Reinhard Schulte⁴, Ana Belchior^{2,5}, Carmen Villagrasa³

1. Departamento de Física, Instituto Superior Técnico, Universidade de Lisboa, Av. Rovisco Pais, 1049-001 Lisboa, Portugal

2. Centro de Ciências e Tecnologias Nucleares (C²TN), Instituto Superior Técnico, Universidade de Lisboa, Estrada Nacional 10, 2695-066 Bobadela LRS, Portugal

3. Institut de Radioprotection et de Sûreté Nucléaire (IRSN), 31 Avenue de la Division Leclerc, 92260 Fontenay-Aux-Roses, France

4. Division of Biomedical Engineering Sciences, Loma Linda University, Loma Linda, CA 92350, USA

5. Departamento de Engenharia e Ciências Nucleares, Instituto Superior Técnico, Universidade de Lisboa, Av. Rovisco Pais, 1049-001 Lisboa, Portugal

* Corresponding Author: joaofcanhoto@tecnico.ulisboa.pt

Abstract

Objective. This study aims to evaluate the influence of the computational algorithm used in calculating conditional ionisation cluster size distributions (ICSD) and associated nanodosimetric parameters from proton track structures obtained with Geant4-DNA Monte Carlo simulations. **Approach.** The Uniform Sampling (US) and Associated Volume (AV) sampling algorithms and the DBSCAN clustering algorithm were used to calculate the ICSD conditioned on cluster sizes $\nu \geq 1$. In the AV algorithm, we explored two configurations: one where sampling volumes could overlap, and ionisations could be counted multiple times (“AV-Overlap”) and one where volumes could not overlap (“AV-No Overlap”). The ICSD of the AV-Overlap configuration was corrected with the weight function $w(\nu) = \nu^{-1}$ to eliminate the bias towards regions of high density of ionisations. In the sampling algorithms, clusters were defined as the number of ionisations in spheres of 3.4 nm in diameter. In DBSCAN, clusters were formed according to a proximity criterion (maximum distance of 3.4 nm) between a minimum number of ionisations (two) and no additional geometrical restrictions were applied. The conditional ICSD, the mean cluster size $M_1^{C_1}$ and the complementary cumulative frequencies $F_k^{C_1}, k \in [2,7]$ were compared. We considered differences in the mean difference larger than two standard deviations statistically significant. **Main Results.** Overall, differences between the AV-No Overlap and the corrected AV-Overlap configurations and between the US and AV sampling algorithms were statistically significant but relatively small, except when statistical fluctuations were large. DBSCAN, as expected, always resulted in significantly larger mean cluster sizes. **Significance.** We showed that the fast and efficient AV-Overlap algorithm can be used instead of the relatively inefficient US algorithm to calculate conditional ICSDs without significant loss of accuracy. The differences observed

between DBSCAN and the other algorithms are understood and originate in the fact that while the scoring volume is fixed for the sampling algorithms, for DBSCAN, it evolves according to the distance between ionisations.

Keywords

Nanodosimetry, Monte Carlo track-structure simulations, Geant4-DNA, computational algorithms

1. Introduction

Monte Carlo (MC) simulations are numerical computational techniques that employ statistical random resampling and are particularly valuable for solving, among others, problems that would be either analytically intractable or experimentally impossible, time-consuming, or too costly (Harrison, 2010; Naqa, Pater and Seuntjens, 2012). In radiation physics, Monte Carlo Track Structure (MCTS) codes, such as CPA100, KURBUC, Ptr, and Geant4-DNA (Grosswendt and Waibel, 1978; Terrissol and Beaudré, 1990; Uehara, Nikjoo and Goodhead, 1993; Incerti, Baldacchino, et al., 2010; Incerti, Ivanchenko, et al., 2010; Bernal et al., 2015; Incerti et al., 2018), have become established tools in micro- and nanodosimetry to study the interaction of ionising radiation with micro- and nanoscopic targets, respectively, such as a cell nucleus or the DNA molecule (Incerti *et al.*, 2016). Differently from the general-purpose codes, like PENELOPE, EGSnrc or Geant4 (Baró *et al.*, 1995; Kawrakow *et al.*, 2000; Agostinelli *et al.*, 2003; Allison *et al.*, 2006, 2016), which use the Condensed History (CH) approach (Dingfelder, 2012), Track Structure (TS) codes simulate the interaction of charged particles, particularly electrons often produced as secondary particles, on an event-by-event basis and down to the eV or sub-eV thresholds (Nikjoo *et al.*, 2006). The result is a detailed description of the particle's track, including the spatial distribution of interaction points and their nature (Dingfelder, 2012).

Nanodosimetry is focused on the characterisation of the ionisation component of the particle track structure with nanometric resolution, either by simulations (MCTS codes) or experimental measurements (nanodosimeters), and seeks to establish the metrological basis for predicting the biological effects of radiation (Rabus *et al.*, 2014; Palmans *et al.*, 2015; Conte *et al.*, 2018). The fundamental quantity in nanodosimetry is the ionisation cluster size, ν , a stochastic quantity that represents the number of ionisations produced by a primary particle and its secondaries in a specific nanometre-sized target volume. The frequency distribution of ν , also the ionisation cluster size distribution (ICSD, $f(\nu)$), and associated nanodosimetric parameters are then used to characterise a radiation field (Palmans *et al.*, 2015).

In computational nanodosimetry, different algorithms have been proposed and used to calculate ICSDs, and we can generally group them into two classes: “sampling” and “clustering”. Sampling algorithms for nanodosimetry use sensitive volumes that score the number of ionisations around the particle track. Clustering algorithms, on the other hand, form ionisation clusters using predetermined criteria with the aim to predict DNA damage; they were first introduced by Nikjoo with the K-Means algorithm (Nikjoo *et al.*, 1998; Pszona, Bantsar and Nikjoo, 2006). More recently, the DBSCAN clustering algorithm has become the preferred choice for simulating radiation-induced DNA damage using Geant4-DNA, often associated with a preselection of the ionisations with a DNA geometry (Francis, Villagrasa and Clairand, 2011; Dos Santos *et al.*, 2013; Marta Bueno *et al.*, 2015).

The most common sampling algorithm in nanodosimetry, also used in this work, is the “Uniform Sampling” (US). In this algorithm, the centre position and, if necessary, the orientation of the sampling volumes inside the volume that bounds the track (scoring region) are generated using a uniform random number generator. The positions can be either generated before or after

the simulation, but the important aspect is that they are independent of the location of interaction points. Some of the previous works that have used this algorithm in nanodosimetry include the works of Alexander, Bueno and Ramos-Méndez (Alexander *et al.*, 2015; M. Bueno *et al.*, 2015; Ramos-Méndez *et al.*, 2018). This algorithm, however, is known to be inefficient in terms of computation time since most sampling volumes will not score any interaction (Famulari, Pater and Enger, 2017).

The "Associated Volume" sampling algorithm is a more efficient sampling method that was proposed and discussed by Lea in 1946 (Lea, 1946) and used for microdosimetry in the late 1980s and 1990s (Kellerer, 1985; Rossi and Zaider, 1996). To our knowledge, with this work, we are the first to apply it to nanodosimetry. The algorithm was developed based on the concept of "associated volume of the track", defined as the union of all spheres of radius r that are centred at transfer points (e.g., ionisations). From this definition, any sphere of radius r whose centre lies within the associated volume will score at least one ionisation, and, therefore, the algorithm has a sampling efficiency of precisely one. The algorithm works iteratively: each iteration consists of 1) randomly selecting an ionisation point, 2) placing the centre of a sphere of radius r at one uniformly randomly generated point that is within the distance r of the selected ionisation, and 3) counting the number of ionisations within the sphere.

The third algorithm used in this work was DBSCAN (Density-Based Spatial Clustering of Applications with Noise), a density-based clustering algorithm introduced in 1996 (Ester *et al.*, 1996). The algorithm forms clusters of arbitrary shapes from spatial data based on two input parameters: *Eps*, a maximum distance from a point that, together with a chosen distance function, defines the neighbourhood region of that point, and *MinPts*, the minimum number of points inside said region required to form a cluster. As the AV algorithm, DBSCAN works iteratively: the position of ionisations is stored in a data structure, such as a vector or a set; the algorithm starts on the first element and iterates until the last element, validating, in each iteration, if there are *MinPts* within the neighbourhood of the selected element to form a cluster. In each iteration, it also validates if any of the *MinPts* within the neighbourhood or if the selected element is already attributed to a cluster: this validation can lead to the extension of an existing cluster or the merging of two existing clusters. The choice of the distance function depends on the application, but, in general, for nanodosimetry, one chooses the Euclidean distance.

To date, there has been no direct comparison of sampling and clustering algorithms for nanodosimetric ICSDs. The main goal of this work was a direct comparison of the ICSDs and associated parameters obtained with Uniform Sampling (US), Associated Volume (AV) and DBSCAN. In addition, we explored whether the equivalence between the US and AV algorithms, previously observed for microdosimetry (Famulari, Pater and Enger, 2017), also holds for nanodosimetric quantities. To achieve these goals, we obtained the ICSD conditioned on clusters with one or more ionisations, $f^{C_1}(v)$, of protons of different initial kinetic energies travelling in a micrometre-sized liquid water box and calculated and compared a set of nanodosimetric parameters.

2. Materials and Methods

2.1. Sampling and clustering algorithms

In the context of radiobiology, DNA lesions are the starting point for radiobiological consequences: double-strand breaks (DSBs), defined as two single-strand breaks (SSBs) not more than ten base pairs or 3.4 nm apart on opposing DNA strands, are considered the most biologically consequential DNA damage (Lazarakis *et al.*, 2012). In sampling algorithms for nanodosimetric studies, it is common practice to approximate the sensitive volume by a cylinder of 3.4 nm in height and 2.3 nm in diameter (Grosswendt, 2005; Lazarakis *et al.*, 2012). However, in this work,

we opted to use the simpler geometry of a sphere of 3.4 nm in diameter. The sphere may be preferred over a cylinder because it has no preferential axis, eliminating the necessity to place sensitive volumes with random orientations. The following subsections provide detailed information about modifications and unique aspects we have introduced in each algorithm for our study.

2.1.1. Uniform Sampling

In “Uniform Sampling” (US), sampling volumes are placed and, if necessary, oriented randomly inside the scoring geometry, usually in a non-overlapping fashion.

In this work, 10^6 non-overlapping spheres of 3.4 nm in diameter were randomly placed inside the scoring region ($1 \mu\text{m}^3$ cube). A sensitive volume was deleted and resampled if it overlapped with another. During the placement procedure, a sequential numeric ID (SVID) was assigned to each sensitive volume. The location of the sensitive volumes was the same for all events.

Whenever an ionisation occurred (by the primary or secondary particles) inside one of the sensitive volumes, we registered the current *eventID* and the volume’s *SVID* in the output file.

2.1.2. Associated Volume

In the Associated Volume sampling algorithm, sampling volumes are placed, iteratively, in the scoring region at random locations that are no more than a distance r apart from an ionisation. In our work, as justified in the beginning of section 2.1, r was set to 3.4 nm. Figure 1 displays a schematic representation of an iteration. In the following bullet points, we describe additional details of our implementation of the algorithm:

1. We considered two configurations for this algorithm:
 - a) In the first configuration, different sensitive volumes can overlap (henceforth, “AV-Overlap”). In this case, no further validation is necessary. The algorithm counts the number of ionisations inside the sensitive volume and stores this number and the position of the centre of the sensitive volume in the output file. Therefore, one ionisation can contribute to more than one sensitive volume.
 - b) In the second configuration, sensitive volumes cannot overlap (henceforth, “AV-No Overlap”). A validation step is necessary to ensure the new sensitive volume does not overlap (totally or partially) with any sensitive volume that has been previously placed. If there is no overlap, the algorithm keeps the sensitive volume; if there is an overlap, the algorithm discards the new sensitive volume and starts a new iteration. At the end of each iteration, the algorithm removes the ionisations inside the new sensitive volume from the list of ionisations for future iterations. For this configuration, it is possible that some ionisations are not included in any sensitive volume when the algorithm terminates.
2. We implemented the following conditions that will terminate the algorithm:
 - i. The number of sensitive volumes equals the number of ionisations.
 - ii. No ionisations remain for random selection.
 - iii. The number of iterations reaches a preset maximum (In this work, the maximum number was three times the number of ionisations in the event).

Note that condition ii. does not apply to the AV-Overlap. For AV-No Overlap, conditions i. and ii. can occur simultaneously. Condition iii. is a fail-safe termination to ensure the algorithm does not enter an infinite loop.

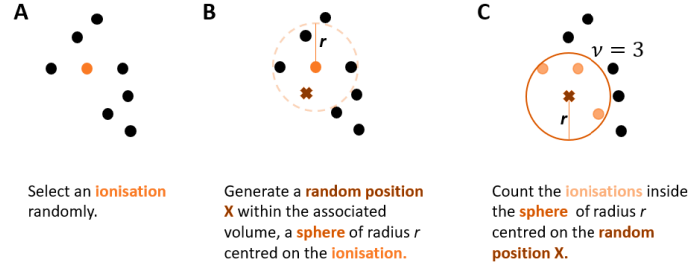


Figure 1. Steps in a single iteration of the “Associated Volume” sampling algorithm: A) an ionisation is randomly selected (orange dot) from *all* ionisations (black dots); B) A point (X) in the sphere of radius r (dashed circle) centred at the selected ionisation (orange dot) is randomly generated; C) If the necessary conditions are met (depending on the chosen configuration), the centre of the new sensitive volume (solid line circle) is placed at point X, and the ionisations inside the volume are counted; in the example, there are three ionisations inside the volume, resulting in a sensitive volume with cluster size $\nu = 3$.

In the Overlap configuration, ionisations can be randomly selected even if they have already been included in a cluster. This, and the fact that the same ionisation can contribute to more than one cluster, introduces a bias in the cluster size distribution, as regions with a higher density of ionisations are more likely to be sampled than those with a lower density. In order to correct the bias, we followed the weighting procedure described in the work of Famulari (Famulari, Pater and Enger, 2017). Briefly, the absolute frequency ICSD, $f(\nu)$, obtained with the Overlap configuration is weighted by a function, $w(\nu)$ that is inversely proportional to the number of ionisations in the cluster, obtaining a cluster size-weighted distribution, $f_w(\nu)$:

$$f_w(\nu) = \nu^{-1} f(\nu) \quad (1)$$

The coordinates of energy depositions resulting in ionisations by the primary proton or secondary electrons in the scoring region were recorded as an array that served as input to the algorithm. At the end of the run, an output file is saved containing the following information: *eventID*, *SVID* (Sensitive Volume ID, a sequential numerical ID assigned to each sensitive volume during runtime), *clusterSize* (the number of ionisations contained in the sensitive volume) and *CX*, *CY* and *CZ* (the x , y , and z coordinates, respectively, of the centre of the sensitive volume).

2.1.3. DBSCAN

DBSCAN is an iterative procedure that forms, extends or merges clusters when a minimum number of points, *MinPts*, lies within the spherical neighbourhood (when using the Euclidean distance) of radius *Eps* centred at given point.

In nanodosimetric studies for radiobiology, often a DNA geometry is used in order to select the ionisation points that fall into the DNA backbone; then, those points are used with DBSCAN setting *Eps* to 3.4 nm, the length of ten DNA base pairs, and *MinPts* to 2, reflecting the minimum number of ionisations usually required to create a DSB. This work also adopted these values but did not perform the preselection of ionisation points with a DNA geometry. Instead, it used all ionisation in the proton tracks on a liquid water homogeneous medium to calculate the ICSDs. The distance function chosen was the Euclidean distance. At the end of the iterative procedure, we considered that each remaining ionisation not included in any cluster was a cluster of $\nu = 1$.

It is relevant to acknowledge that, although the DBSCAN used in this work was derived from the clustering example (“extended/medical/dna/clustering”) available in Geant4-DNA,

which also uses a liquid water homogeneous medium without any DNA geometry, it differs in its implementation. Notably, in the Geant4-DNA example, the input data for the DBSCAN algorithm consists only of the energy deposition events selected based on particular selection criteria (to replace the DNA geometrical criteria) in a phase before the algorithm. Furthermore, in the last step of the example, the clusters can be merged based on the distance between the barycentres of the clusters (Francis, Villagrasa and Clairand, 2011). The version of DBSCAN used in this work does not contain the selection phase and the merging based on the barycentres.

2.2. Proton track simulations

We simulated tracks of protons in liquid water using the Geant4-DNA toolkit based on Geant4 version 11.0. The G4EmDNAPhysics_option2 physics constructor was used for the transport and interaction of particles in liquid water with the proton and hydrogen elastic scattering processes turned off. The selection of the option2 constructor was based on the fact that its dielectric model for electron ionisations provides a broader energy range (up to 1 MeV) than option4 (10 keV) and option6 (250 keV). While option4 is the recommended constructor by the Geant4-DNA collaboration (Incerti et al., 2018), we expect that the results presented here will not significantly change with the choice of the physics constructor.

All simulations used monoenergetic protons as the primary particle. Protons were started with initial kinetic energies of 0.25, 0.5, 0.75, 1, 2.5, 5, 7.5, 10, 25, 50, 75 and 100 MeV. The energies were chosen in order to cover a broad range and achieve an approximately spatially invariant ICSD throughout the scoring volume. The protons were tracked in a square box of $1 \mu m$ side length (scoring region) enclosed by a square box of $1.4 \mu m$ side length (world volume), both composed of liquid water. The protons started 200 nm from the scoring volume and travelled along the $+x$ axis. The centre of both volumes coincided with the origin of the Cartesian coordinate system.

The number of primary particles simulated in the AV–No Overlap, US, and DBSCAN algorithms were adjusted for each of the initial energies so that the simulations resulted in a total number of clusters (in our case, the number of clusters with one or more ionisations) of the same order of magnitude as that obtained with the AV–Overlap method after applying the weight function.

Only ionisations by the primary protons and the secondary electrons were scored.

2.3. Data Analysis

Simulations were performed three times with different initial seeds to assess the statistical uncertainty of the results (standard deviation). A higher number of runs would have mainly impacted the infrequent large clusters, which would not significantly change our results. For this reason, we felt the computational burden added by increasing the number of runs was not justified. The output data files were processed using the R Statistical Software v4.2.3 (R Core Team, 2023).

For each method and proton energy, we derived a run-ICSD from which we calculated the following nanodosimetric parameters:

- a) The first moment, or mean cluster size, M_1 :

$$M_1^{C_1} = \sum_{v=1}^{\infty} v f^{C_1}(v) \quad (2)$$

- b) The complementary cumulative frequencies F_k , with $k \in [2,7]$:

$$F_k^{C_1} = \sum_{v=k}^{\infty} f^{C_1}(v) \quad (3)$$

For each energy, the mean and standard deviation of each parameter for the different sampling and clustering algorithms were compared. We considered differences larger than two standard deviations of the mean difference statistically significant.

In the US and AV methods, we further considered the execution time and the sampling efficiency in the analysis. We used the function *GetRealElapsed()* from the *G4Timer* class to extract the “real elapsed time” of each run. The timer started during the *BeginOfRunAction()* and stopped at the end of the *EndOfRunAction()* after Geant4 wrote and closed the output files. Each run consisted of two steps: 1) particle transport and interaction simulation and 2) sampling algorithm. The time spent in the construction of the geometry is not considered. The measured time includes the time spent in both steps and, therefore, allows a direct comparison of the execution time of both AV configurations and AV and US algorithms. We performed the simulations using eight cores on an Intel Core i7 CPU @ 3.40 GHz and a multithread build of Geant4 with eight threads. Sampling efficiency was defined as the ratio of the number of sensitive volumes (SVs) with at least one ionisation to the total number of SVs.

3. Results

The Results section is organised in the following way: section 3.1 compares the Overlap and the No Overlap configurations of the Associated Volume (AV) algorithm. Section 3.2 compares the AV - No Overlap algorithm to the Uniform Sampling (US) algorithm. Section 3.3 compares both sampling algorithms to the DBSCAN clustering algorithm.

3.1. Associated Volume: Overlap vs. No Overlap

3.1.1. ICSD and associated parameters

Figure 2 shows the ICSDs for three of the twelve energies simulated. Each point represents the mean of the three independent runs, and error bars represent two standard deviations of the mean. It is observed that for cluster of one ionisation, frequencies are always higher for the No Overlap configuration compared to the unweighted Overlap configuration. The frequency difference is energy-dependent for cluster of two and three ionisations. On the other hand, for clusters of four or more ionisations, the unweighted Overlap configuration consistently yields higher frequencies than the No Overlap configuration. The Overlap configuration, coupled with the possibility of counting ionisations multiple times, favours regions of higher ionisation density, which explains the observed higher frequency of large clusters relative to single ionisations. These two conditions also lead to a larger observed maximum value of the cluster size for most proton energies.

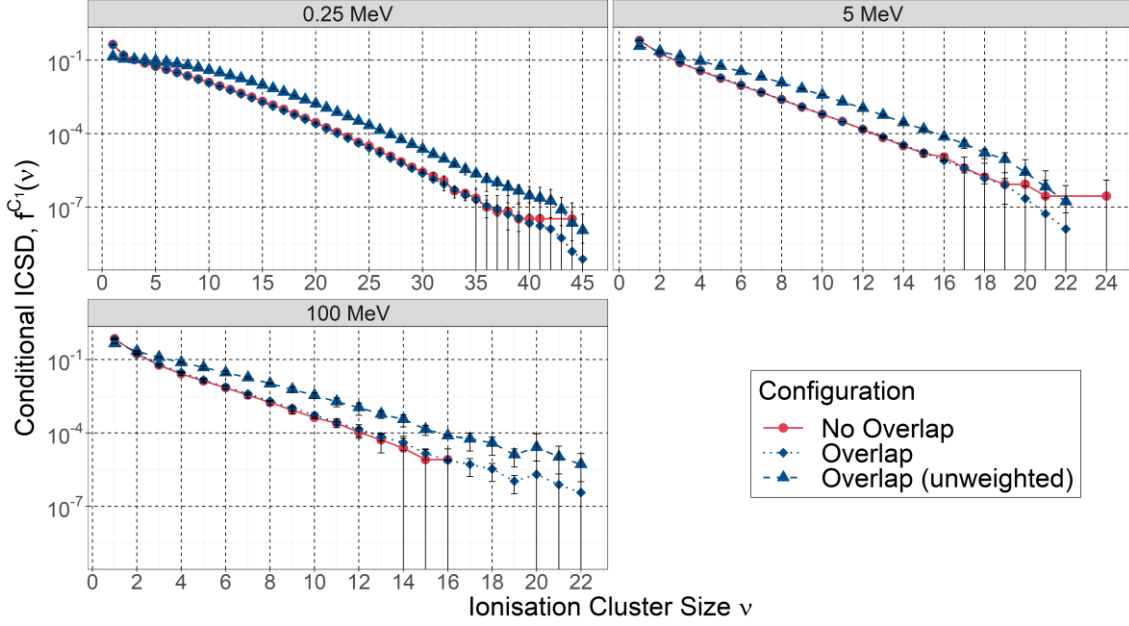


Figure 2. ICSD conditioned on cluster sizes equal to or greater than one ionisation for the AV in the No Overlap (solid line, red dots), unweighted Overlap (dashed line, blue triangles) and weighted Overlap (dotted line, blue diamonds) configurations obtained after the simulation of 0.25 MeV (top left), 5 MeV (top right) and 100 MeV (bottom left) protons. The distributions are the mean of three independent runs, and the vertical error bars indicate two standard deviations of the mean. Lines are a guide for the eye.

The following logical arguments can explain the observed fact that the maximum detected cluster size is generally smaller for the No Overlap configuration. Two conditions must occur to score a maximum-sized cluster in a high-density region: 1) a point suitable for containing that maximum-size cluster is randomly selected (step B in Figure 1), and 2) the associated volume sphere does not overlap with other spheres. However, for the No Overlap configuration, the actual volume available for sampling becomes progressively smaller after each iteration resulting in a new cluster. Therefore, the combined probability of “selecting a suitable centre point and the cluster does not overlap” also becomes progressively smaller. On the other hand, for the Overlap configuration, the likelihood of scoring a maximum-sized cluster depends only on the probability of selecting a suitable centre point because the volume available for sampling is constant. The conditions under which the scoring of large clusters is possible are less restrictive for Overlap than for No Overlap, which explains the observed trend.

As mentioned in 2.1.2, the bias towards regions of high density of ionisations needs to be corrected. We can obtain an unbiased ionisation cluster size distribution by weighting the frequency of each cluster size by the inverse of the number of ionisations in the cluster (equation (1)). As shown in Figure 2, the corrected ICSD agrees well with the ICSD of the No Overlap configuration and is mostly within two standard deviations of the mean frequencies. In the remaining results of this subsection, we will only consider the corrected Overlap and the No Overlap configurations.

Mean Cluster Size and Complementary Cumulative Frequencies

The upper plot on the left in Figure 3 shows the first moment of the conditional ICSD, M_1^{C1} , for the Overlap and the No Overlap configurations as a function of the initial kinetic energy of the primary proton. The values are the mean of the mean cluster sizes of three independent runs, and the vertical error bars represent two standard deviations of the mean. The lower plot on

the left shows the ratio of $M_1^{C_1}$ of the Overlap configuration to that of the No Overlap configuration.

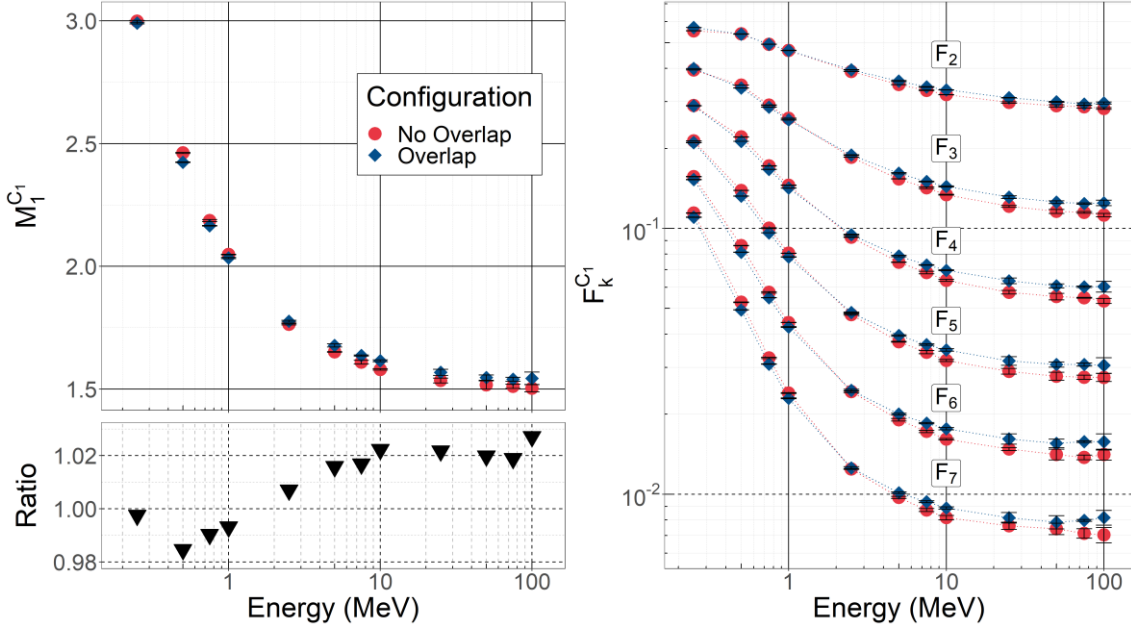


Figure 3. Left Upper plot: First moment of the conditional ICSD as a function of the initial kinetic energy of the primary proton using the No Overlap (red dots), and Overlap (blue diamonds) configurations of the AV algorithm. Left Lower plot: Ratio of $M_1^{C_1}$ calculated with the Overlap configuration to that calculated with the No Overlap configuration. Right: Complementary cumulative frequencies $F_k^{C_1}$, $k \in [2, 7]$ of the conditional ICSD using the AV sampling algorithm in the No Overlap configuration (red dots) and Overlap configuration (blue diamonds). Lines are guide for the eye. The values are the mean of three independent runs, and vertical error bars indicate two standard deviations of the mean.

As expected, once the Overlap configuration is properly corrected for bias, the mean cluster sizes obtained using this configuration agree very well with those obtained using the No Overlap configuration. For comparison, the unweighted Overlap configuration resulted in mean cluster sizes that were 1.6 to 1.9 times larger than those of the No Overlap configuration (results not shown). The absolute differences between the two configurations range from 0.007 to 0.04. Per our analysis assumptions, the differences in the mean cluster size calculated using both configurations are statistically significant for all energies; however, the differences are minor and relative differences expressed as a percentage of the No Overlap configuration are predominantly within 2% (Figure 3, left lower plot).

The right plot in Figure 3 shows the complementary cumulative frequencies $F_k^{C_1}$, $k \in [2, 7]$, of the conditional ICSD for the Overlap and the No Overlap configurations. When considering distributions conditioned on cluster sizes equal to or greater than j ionisations, the complementary cumulative frequency $F_{k=j}^{C_j}$ is equal to one. Since the distributions we are considering are conditioned on cluster sizes equal to or greater than one ionisation, $F_1^{C_1}$ was not included in our analysis.

As already observed for the mean cluster size, the absolute differences, although larger than two standard deviations of the mean difference for most k values and energy ranges, are relatively minor, ranging from 6.4×10^{-5} to 1.6×10^{-2} . In general, the relative differences between the frequencies $F_k^{C_1}$ of these two sampling configurations increase with the value of k , as is expected because of progressively smaller absolute differences.

It is important to recall that, in our simulations, we imposed the condition that the total number of clusters with size $\nu \geq 1$ had to be approximately the same for the two configurations. Furthermore, the scoring of large clusters is less frequent and subject to more significant statistical fluctuations, particularly when the diameter of the sampling volume is smaller than the mean separation of ionisations. For example, for $F_7^{C_1}$, the relative difference expressed as a percentage of the No Overlap configuration is equal to 3.5% for 0.25 MeV protons and 16.2% for 100 MeV protons. Looking back at the ICSDs in Figure 2, it becomes evident that this value of k corresponds to a region of relatively high frequency for 0.25 MeV protons but intermediate-to-low frequency for 100 MeV protons. Given the range of k considered in this analysis ($k \in [2, 7]$), it would be better to change the condition of the comparable number of clusters to $\nu \geq 7$. This would reduce the impact of statistical fluctuations on $F_k^{C_1}$ for larger k and higher energies, and we expect the true relative differences to be smaller than those observed.

3.1.2. Execution Time

In light of the results presented in the previous subsections, considering the computational cost of the Overlap and No Overlap configurations is important. The left side of Figure 4 shows the execution time for each configuration as a function of the initial kinetic energy of the primary proton between 0.5 MeV and 100 MeV. Due to the different number of events in both configurations, it is also relevant to consider the execution time per event, shown on the right side. The values are the mean of the execution time of three independent runs, and the vertical error bars represent two standard deviations of the mean. The execution time for the Overlap configuration is consistently shorter than the No Overlap for all energies. However, when the execution time per event is considered, we see that the difference between the two configurations is mainly statistically significant at proton energies below 1 MeV. These results show that the Overlap configuration is generally more CPU-demanding for low energy (high LET) particles than the No Overlap configuration.

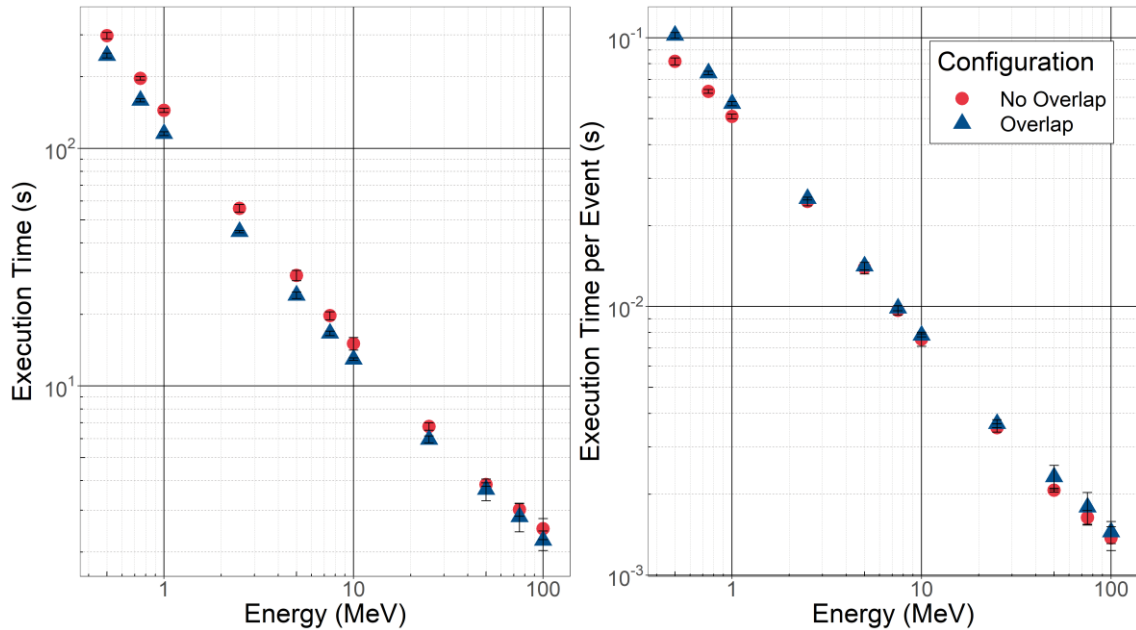


Figure 4. Average execution time (left) and execution time per event (right), in seconds, as a function of the proton's initial kinetic energy for the No Overlap (red circles) and Overlap (blue triangles) configurations. The values are the mean of the execution time of three independent runs, and the vertical error bars indicate two standard deviations of the mean.

The faster execution time and the higher computational cost of the Overlap configuration are explained as follows: the Overlap configuration is designed to generate more clusters per event than the No Overlap configuration. Consequently, it needs fewer primary particles to achieve the same number of clusters in a run. This design, however, directly impacts its performance per event. Consider the ratio of the number of performed iterations to the number of ionisations in the event: irrespective of proton energy, the ratio is, generally, always equal to one for the Overlap configuration, i.e., the algorithm will iterate as many times as the number of ionisations produced in the event. Contrarily, in the No Overlap configuration, this ratio depends on the energy of the primary particle: as the energy increases, ionisations become sparser, and the ratio tends to approach one; as the energy decreases, ionisations become denser, and the ratio tends to decrease. As a result, it usually takes fewer iterations to get the algorithm to finish. Something important to note is the fact that the validation step of checking for overlap in the No Overlap configuration has a negligible effect on the execution time.

3.2. Uniform Sampling vs. Associated Volume

3.2.1. ICSD and associated parameters

Figure 5 shows the conditional ionisation cluster size distributions obtained with the US (purple dots) and AV-No Overlap (red circles) sampling algorithms for three of the twelve energies studied. Each point represents the mean of three independent runs, and vertical error bars represent two standard deviations of the mean. Whereas Uniform Sampling allows the calculation of unconditional and conditional cluster size distributions, the AV method only gives conditional distributions. Therefore, we compared the conditional distributions of both sampling algorithms. The distributions are predominantly in good agreement with no specific trend observed, and overall, the differences are minor and within two standard deviations.

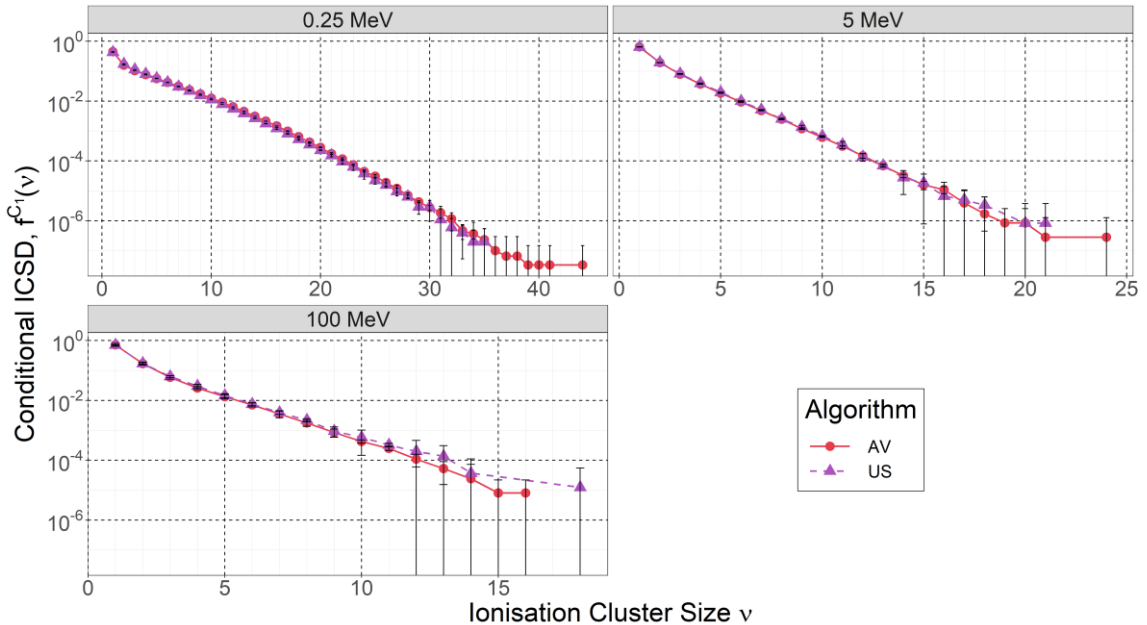


Figure 5. ICSD conditioned on cluster sizes equal to or greater than one ionisation for the AV- No Overlap (solid line, red circles) and Uniform Sampling (dashed line, purple triangles) algorithms after simulation of 0.25 MeV (top left), 5 MeV (top right) and 100 MeV (bottom left) protons. The distributions are the mean of three independent runs, and the vertical error bars indicate two standard deviations of the mean. Lines are a guide for the eye.

Our results do not support a concern that the AV approach, which places the sensitive volumes using the position of ionisations, would introduce a potential bias in the conditional ICSD. This finding is not surprising considering that the conditional ICSD from the US approach only considers sensitive volumes randomly placed that contain at least one ionisation, which are, by definition, placed within the associated volume of the track.

Mean Cluster Size and Complementary Cumulative Frequencies

The upper plot on the left in Figure 6 shows the first moment of the conditional ICSD, $M_1^{C_1}$, for the AV and US sampling algorithms as a function of the initial kinetic energy of the primary proton. The values are the mean of the first moments of three independent runs, and the vertical error bars indicate two standard deviations of the mean. The lower plot on the left shows the ratio of $M_1^{C_1}$ of the AV algorithm to that of the US algorithm.

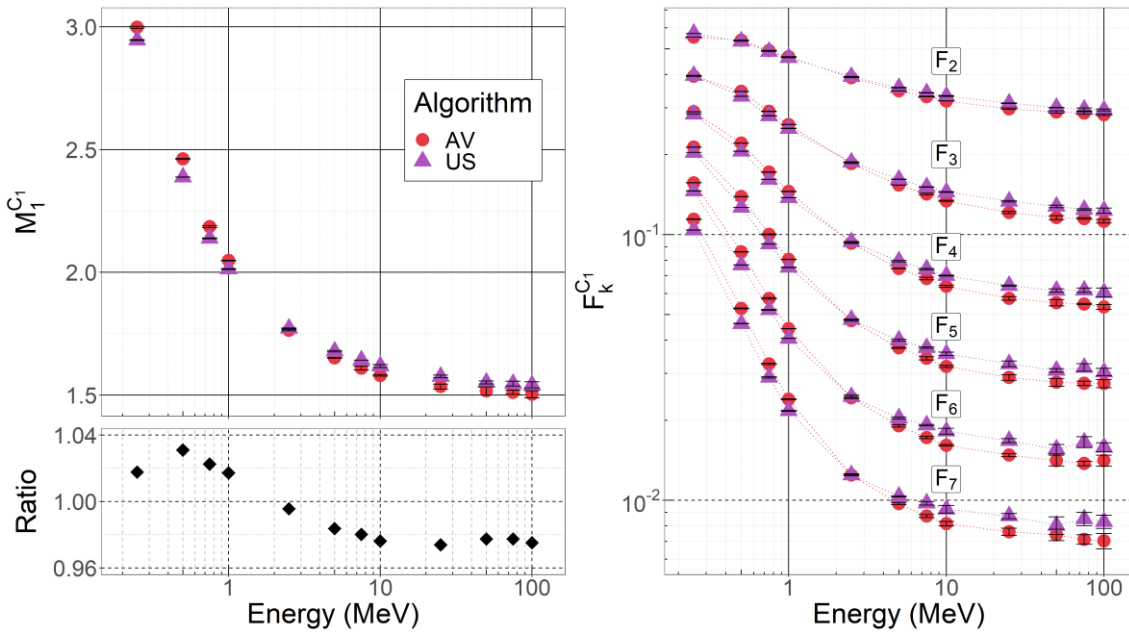


Figure 6. Left: Upper plot: First moment of the conditional ICSD as a function of the proton's initial kinetic energy for the AV–No Overlap (red circles) and US (purple triangles) sampling algorithms. Lower plot: Ratio of $M_1^{C_1}$ calculated with the AV algorithm to that calculated with the US method. Right: Complementary cumulative frequencies $F_2^{C_1}$ to $F_7^{C_1}$ of the conditional ICSD for the AV (circles) and US (triangles) algorithms. Lines are guide for the eye. Each value is the mean of three independent runs, and the vertical error bars indicate two standard deviations of the mean.

For all energies, differences are larger than two standard deviations of the mean difference but relatively small. Absolute differences range from 0.01 to 0.07, and relative differences expressed as a percentage of the US method are predominantly within $\pm 3\%$ (Figure 6, lower plot).

The right plot in Figure 6 shows the complementary cumulative frequencies, $F_k^{C_1}$, $k \in [2, 7]$, of the conditional ICSD for the two algorithms. The absolute differences range from 2.38×10^{-5} to 1.72×10^{-2} . Overall, we observe the same behaviour as in the comparison of the two AV configurations: increasing the value of k also increases the relative difference in the calculated value between the two methods.

For $F_2^{C_1}$, the relative differences between the two methods expressed as a percentage of the US algorithm are equal to or smaller than 4.7%, while for $F_7^{C_1}$, differences are generally higher

than 6%. The discussion of the complementary cumulative frequencies comparing the two AV configurations (see subsection 3.1.1) is also valid here: the higher relative differences for larger k are due to the progressively smaller absolute values and the more significant impact of statistical fluctuations for large cluster sizes. Once again, imposing a more restrictive condition in the comparable number of clusters of both algorithms, such as fixing the number of clusters of $\nu \geq 7$ rather than $\nu \geq 1$, will reduce the impact of statistical fluctuations on $F_k^{C_1}$ for larger k and higher energies and will likely result in smaller relative differences than those observed. Nevertheless, the use of $\nu \geq 1$ provides evidence for the similarity (absolute differences equal to or smaller than 1.72×10^{-2}) of both methods in the computation of complementary cumulative frequencies of conditional ICSDs.

3.2.2. Sampling Efficiency

Figure 7 shows the sampling efficiency of the US method, specific for the geometry setup used in this work, as a function of the initial kinetic energy of the primary proton. The sampling efficiency is energy-dependent, which is expected. As the energy increases, the mean number of ionisations decreases, and so does the number of sensitive volumes that score ionisations.

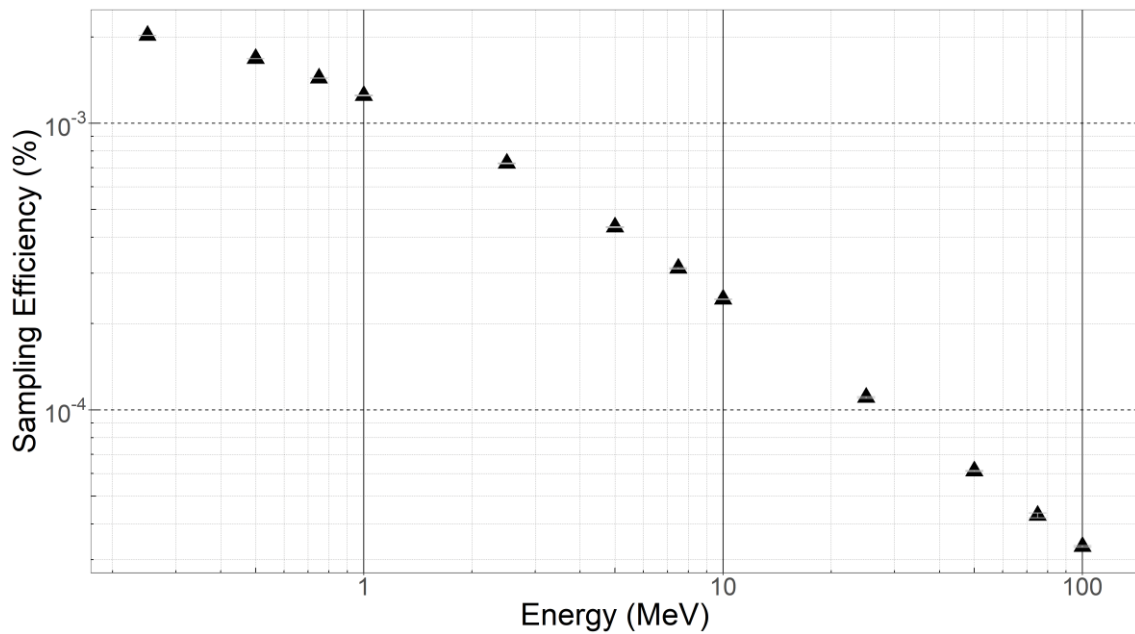


Figure 7. Sampling efficiency as a function of the initial kinetic energy of the primary particle for the Uniform Sampling algorithm. Values are the mean of the three independent runs, and the vertical error bars indicate two standard deviations of the mean.

It is evident that the US algorithm is rather inefficient compared to the 100% efficiency of the AV algorithm. The percentage efficiency of the US algorithm ranges from less than 10^{-2} at the lowest energy to 10^{-5} at the highest energy.

3.2.3. Execution Time

Figure 8 shows the execution time and execution time per event for both algorithms as a function of the initial kinetic energy of the primary proton. As expected, the AV algorithm takes considerably less time to reach the same level of statistical uncertainty and is generally less computationally expensive than the US algorithm.

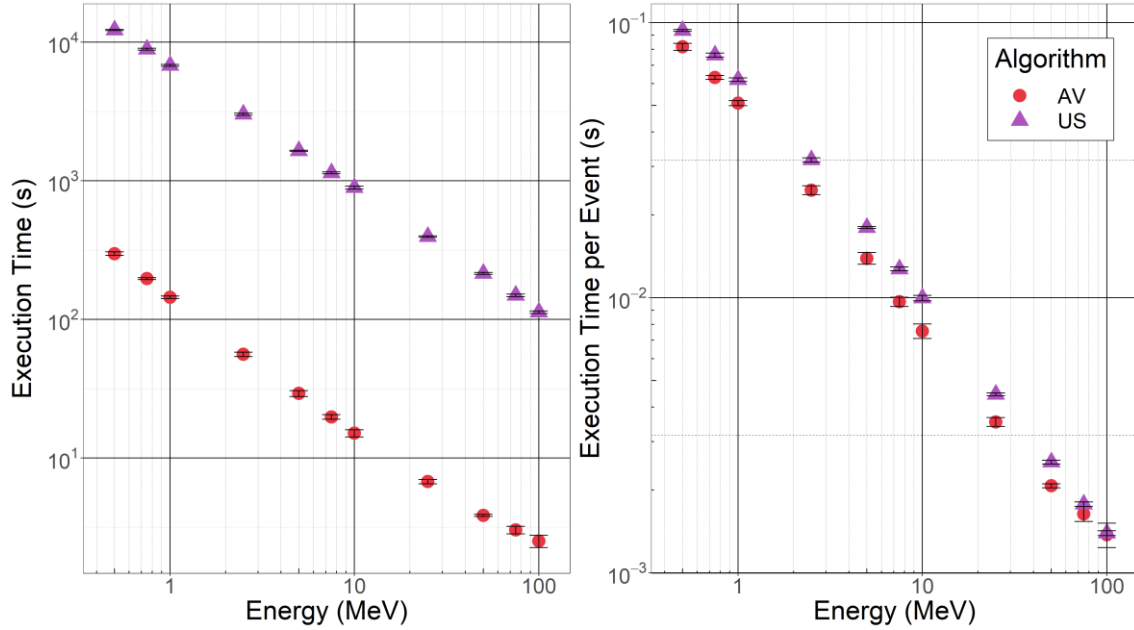


Figure 8. Execution time (left) and execution time per event (right) for the AV (red circles) and the US (purple triangles) algorithms as a function of the proton’s initial kinetic energy. Values are the mean of three independent runs, and vertical error bars are two standard deviations of the mean.

The longer execution times of the US algorithm result from the need to simulate a higher number of primary particles to achieve the desired level of statistical uncertainty, which is a direct consequence of the low sampling efficiency. Furthermore, it is also more computationally expensive for most of the energies used in this work.

It is important to note that the plotted execution time of the US algorithm does not include the time spent placing the sensitive volumes. When including it, the differences between the methods become even larger.

3.3. DBSCAN vs. Sampling

The left plot on Figure 9 displays the ionisation cluster size distribution obtained using the US, AV and DBSCAN algorithms for protons with initial kinetic energy of 5 MeV. Overall, the behaviour is the same for all energies, so, for simplicity, only one energy is shown. The DBSCAN tends to underestimate the frequency of single-event clusters and to overestimate the frequency of larger clusters in comparison to the distributions of the sampling algorithms. More importantly, with DBSCAN the distributions always extend to cluster sizes that are, in general, two to ten times larger than the larger cluster size found in the sampling algorithms. The right plot in Figure 9 shows the mean cluster size of the conditional ICSD for all twelve energies studied in this work. The values are the mean of the mean cluster sizes of three independent runs, and the vertical error bars indicate two standard deviations of the mean. DBSCAN, as expected, following the analysis of the ICSD, consistently results in mean cluster sizes larger than those obtained with the US and AV algorithms. For example, the value for $M_1^{C_1}$ obtained with DBSCAN is 15 and 1.7 times higher than those reported using the sampling algorithms for the lowest and highest simulated energies, respectively.

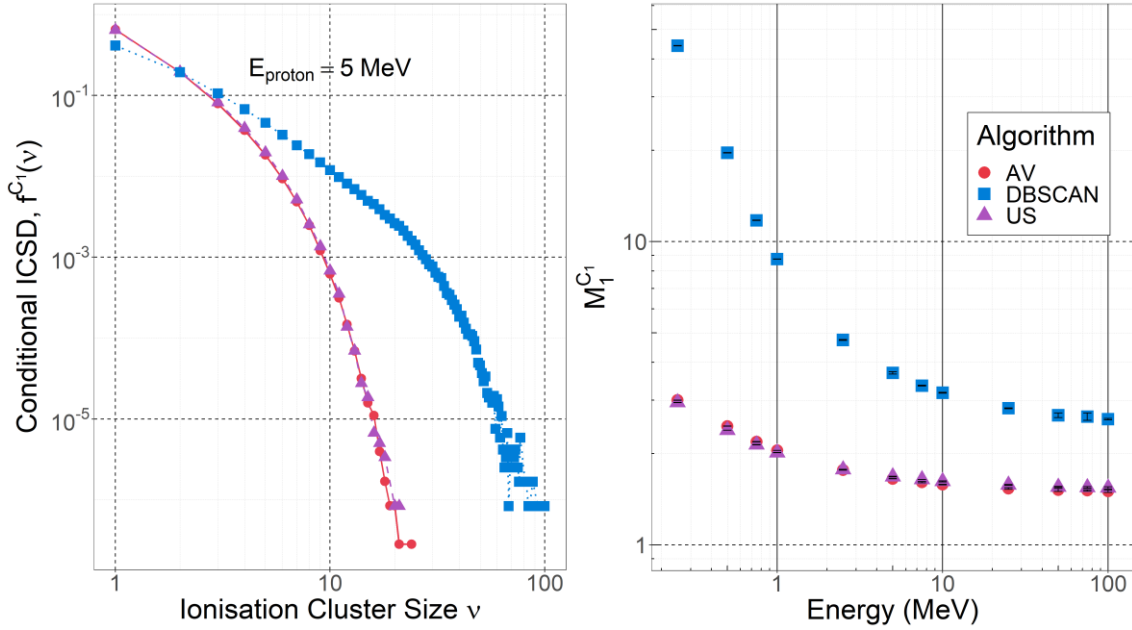


Figure 9. Left: ICSD conditioned on cluster sizes equal to or greater than one ionisation for the DBSCAN (dotted line, blue squares) clustering algorithm and the AV (solid line, red circles) and US (dashed line, purple triangles) sampling algorithms after simulation of 5 MeV protons. The distributions are the mean of three independent runs. Lines are a guide for the eye. Right: First moment of the conditional ICSD obtained with the DBSCAN clustering algorithm (blue squares) and the AV (red circles) and US (purple triangles) sampling algorithms as a function of the initial kinetic energy of the primary proton. The values are the mean of three independent runs, and the vertical error bars indicate two standard deviations of the mean.

These results were expected but not yet quantified. In order to understand the much larger mean cluster sizes observed with DBSCAN, it is essential to recall that this algorithm forms ionisation clusters solely based on a minimum number of ionisations (in our case, two) within a certain distance (Eps). Unlike the sampling algorithms, clusters in DBSCAN can grow beyond the starting distance Eps because of extension and merging, and, therefore, they are not limited by a fixed geometric volume. Thus, the DBSCAN results give a better view of the size of the clusters formed in the (continuous) water medium, while the results presented before correspond better to what would be measured by a defined volume detector.

Figure 10 shows the mean distance between an ionisation and the barycentre of its cluster as a function of the initial kinetic energy of the primary proton. The dashed line indicates the value set for the input parameter Eps (3.4 nm), and the dotted-dashed line indicates the radius of the sampling sphere used in the sampling algorithms ($r = 1.7$ nm). For energies below 10 MeV, the mean distance from the barycentre is larger than the radius of the sampling volumes. For energies below 1 MeV, that distance is also larger than the input parameter Eps . For 0.25 MeV, the mean distance is almost ten times the input parameter Eps and twenty times the radius of the sampling sphere.

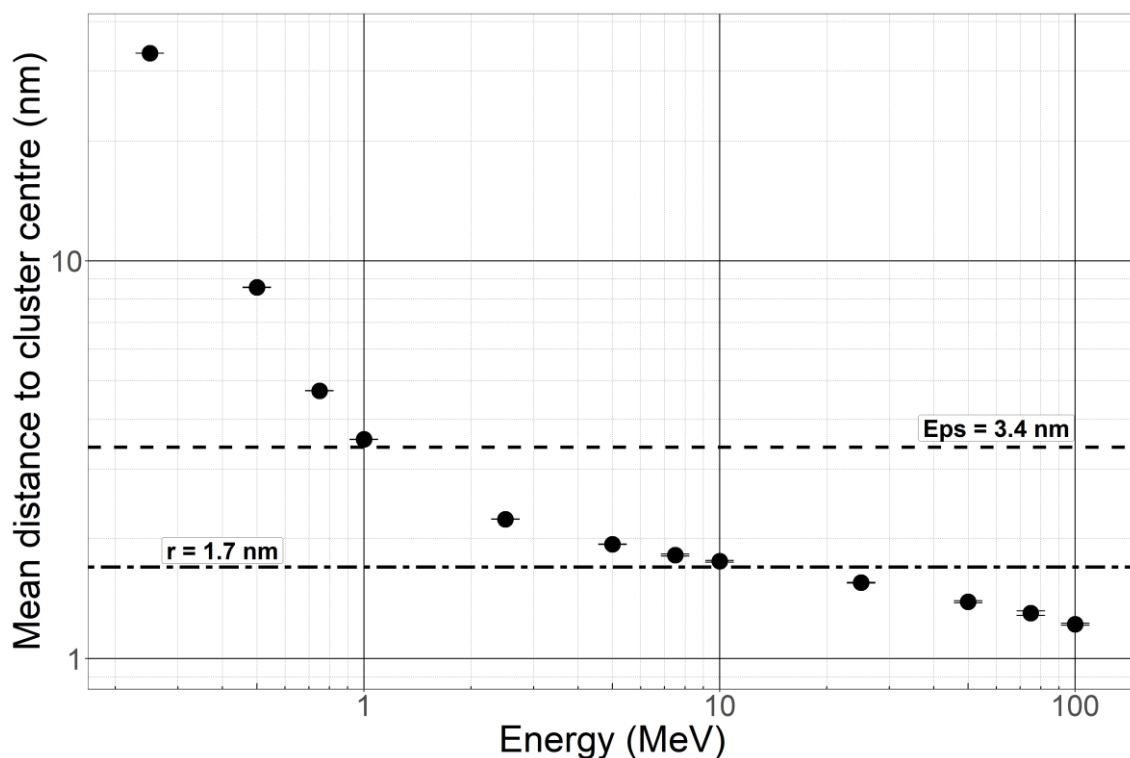


Figure 10. Mean distance between an ionisation and the barycentre of its cluster as a function of the initial kinetic energy of the primary proton. The dashed horizontal line represents the input parameter Eps of 3.4 nm, and the dotted-dashed horizontal line represents the 1.7 nm radius of the sampling sphere (r) for reference.

4. Discussion

This study aimed to compare and investigate the differences in conditional ionisation cluster size distributions (ICSD) and related nanodosimetric quantities using different sampling and clustering algorithms from the literature with Geant4-DNA Monte Carlo track structure simulations. More specifically, we used the widely adopted algorithms Uniform Sampling (US), in which small sampling volumes are uniformly and randomly distributed inside the scoring region, and DBSCAN, a clustering algorithm that clusters spatial data according to a defined minimum number of points within a certain distance. Although widely used, the US algorithm is known to be inefficient for calculating conditional ICSDs because most of the sampling volumes will not score ionisations. For that reason, we have employed, for the first time in computational nanodosimetry, an algorithm based on the concept of the associated volume of the track, the Associated Volume (AV) sampling algorithm, in which the random distribution of the sampling volumes takes into consideration the position of ionisations. We further extended this algorithm by considering two different configurations: the standard configuration, “AV–Overlap”, where the sampling volumes can overlap, and the ionisations can contribute to more than one cluster, and a new configuration, “AV–No Overlap”, where the sampling volumes cannot overlap.

In the US and AV sampling algorithms, clusters were defined as the number of ionisations in spherical volumes of 3.4 nm in diameter, whereas, in the DBSCAN clustering algorithm, clusters were formed according to a proximity criterion (maximum distance of 3.4 nm) between a minimum number of ionisations (two ionisations) but without any prior section of points, contrary to what is generally done when it is used to link these clusters to radiation-induced biological damage. Isolated ionisations at the end of the DBSCAN algorithm were considered “single-ionisation clusters”. For all algorithms studied, we considered the ionisation cluster size distribution conditioned on cluster sizes equal to or greater than one ionisation.

In comparing the AV configurations, Overlap and No Overlap, we showed that when the bias in the Overlap is not corrected, the configuration results in large differences in ICSDs. However, when the ICSD is weighted by the inverse of the cluster size, the differences in the nanodosimetric parameters, while remaining statistically significant, are generally smaller than 5% except for the complementary cumulative frequencies associated with large k values, which are dominated by large statistical fluctuations.

When we compared the US with the AV–No Overlap, again, we found relative differences larger than two standard deviations of the mean difference in some of the ICSDs and the parameters derived from them. However, these differences were generally within a few percent except for the complementary cumulative frequencies associated with large k values, where random fluctuations dominated.

In summary, these results show that, with the same fixed maximum volume of the cluster, we can use the AV algorithm in its corrected Overlap configuration to calculate conditional ICSDs and associated parameters with an accuracy comparable to the US algorithm but with a significant decrease in computation time.

Differences in the mean cluster size between the AV and US sampling algorithm and the DBSCAN clustering algorithm were always significantly larger than two standard deviations. DBSCAN resulted in mean cluster sizes 1.7 to 15 times higher than the values obtained with the sampling algorithms, which is explained by the fact that clusters in our general implementation of DBSCAN were not geometrically confined.

The primary purpose of this study was to evaluate the differences and similarities observed between algorithms used in computational nanodosimetry rather than recommending a particular algorithm for the entire spectrum of applications of nanodosimetry. As this work continues, particular algorithms may be developed for applications of nanodosimetry, such as treatment planning and radiation protection. Although computational efficiency is an important aspect of computational nanodosimetry, one should strive to confirm that the measured ICSD produced by these algorithms are consistent 1) with ICSD measured by experimental nanodosimeters, see, e.g., previous works by Garty and Bashkirov (Garty *et al.*, 2002; Bashkirov *et al.*, 2009), and 2) with predicted biological endpoints, see, e.g., the works by Garty and Conte (Garty *et al.*, 2010; Conte, Bianchi and Selva, 2023).

For example, in the context of comparing theoretical and experimental nanodosimetric ICSDs obtained with a fixed sensitive volume, sampling algorithms lend themselves as a logical choice for validation purposes and performance simulations of the nanodosimeters. Typically, established experimental nanodosimeters comprise an ionisation volume (IV) containing a low-pressure gas and a single equivalent nanometre-sized sensitive volume that samples individual charged particle tracks inside the IV (Palms *et al.*, 2015; Rucinski, Biernacka and Schulte, 2021). As we did in this work, having multiple randomly charged particle tracks passing the IV is, therefore, computationally equivalent to sample a single track with multiple sampling volumes. It is important to note that, different from the Monte Carlo simulated data used in this work, experimental nanodosimetric data required further consideration of ionisation detection efficiency and its spatial distribution (sensitive volume maps) (Schulte *et al.*, 2006)

In the application of clustering and sampling of ionisations to radiobiology, the absence of a fixed volume in DBSCAN can present a significant advantage over a constant sampling volume to score ionisation clusters. Sensitive volumes of fixed size discretely sample the track and may split large clusters into smaller ones, which are biologically less relevant. On the other hand, since large clusters are the precursors of complex DNA damage to a certain degree, failing to capture those would be a limitation of sampling algorithms, particularly for low-energy charged particles. In the DBSCAN version used in this work, clusters were allowed to grow in any direction without limits. This limitless growth disregards the actual geometry of the DNA molecule and the water molecules immediately bound to or surrounding the DNA, which can

contribute to indirect radiation damage. Although the folded DNA molecule is randomly oriented in the cell nucleus, it is directionally organised, approximating cylindrical sections. Ionisations may be in close spatial proximity but located in separated DNA segments. In this case, they would not form complex damage. This is the reason why a selection of ionisation points is necessary prior to the use of DBSCAN in radiobiological applications. This selection can be done by limiting the extension of an ionisation cluster along the axis of a cylindrical region. Previous studies, e.g. (M. Bueno *et al.*, 2015; Meylan *et al.*, 2017; Nicolas Tang *et al.*, 2019; N. Tang *et al.*, 2019), have implemented a two-step approach with DBSCAN. Using a realistic description of the DNA double-helix structure with defined sensitive regions, ionisations that did not occur within those regions were disregarded. The list of the remaining ionisations was then used as input for DBSCAN. Although this approach introduces further complexity in the simulations, it may capture the true radiobiological relevant clusters more accurately.

Another critical aspect of the sampling algorithms concerns the shape and dimension of the sampling volume. In computational nanodosimetric studies, the standard practice is to use a cylinder of 3.4 nm in height and 2.3 nm in diameter as the sampling volume. This cylinder approximates a ten base-pairs DNA segment, where the length of ten base-pairs (3.4 nm) is considered the limiting distance between individual DNA lesions to form a single DNA damage. In this work, however, we deviated from this practice for computational reasons and used a spherical sampling volume with a diameter equal to 3.4 nm. Although the cylinder and its dimensions came from practical knowledge, its use, like any other shape or dimension, still lacks experimental comparison and validation.

The consistency of nanodosimetric parameters predicting experimental radiobiological data may inform on the choice of shape and dimension of sensitive volumes and other parameters in sampling and clustering algorithms. From a practical point of view, one should continue to develop algorithms and use sampling volumes that are computationally efficient and compare them in terms of their predictive power.

Among the three algorithms studied here, the current implementations of the AV sampling algorithm and the DBSCAN clustering algorithm present a practical limitation. In a mixed radiation field, i.e., a field that comprises different particles with different energies, such as those found in radiotherapy, the resulting ionisation cluster size distribution can be calculated by a fluence weighted sum of the individual distributions of each particle due to the approximately additive property of nanodosimetric probability distributions (Conte, Bianchi and Selva, 2023). However, this is only valid for *unconditional* ICSDs, and the implementations of the AV and DBSCAN algorithms presented in this work result in *conditional* ICSDs. A study by Ramos-Méndez that explored the addition of conditional ICSDs in a macroscopic volume exposed to a mixed particle therapy radiation field found that conditional ICSDs did not produce useful results for treatment planning (Ramos-Méndez *et al.*, 2018). Therefore, *unconditional* ICSDs are required in mixed radiation fields. Our work showed a high degree of similarity of conditional ICSD derived by using the US and AV sampling algorithms. With the possibility of counting the number of volumes with no ionisations using the US algorithm, our results motivate us to investigate the possibility of deriving unconditional ICSD using a novel, yet efficient, way to combine the US and AV algorithms.

5. Conclusions

The dependence of ionisation cluster size distributions and related nanodosimetric quantities on the choice of computational algorithm was investigated for protons of different energies. The often-used Uniform Sampling (US) and DBSCAN algorithms were compared to the more efficient Associated Volume (AV) sampling algorithm. We demonstrated that the choice of sampling algorithm does not introduce discrepancies larger than a few percent in conditional

ionisation cluster size distributions and their first moment. The complementary cumulative frequencies, on the other hand, showed that the relative differences increased with the threshold k . However, statistical fluctuations of large cluster sizes at higher k likely influenced this result. Given the similarities observed between the sampling algorithms, the AV algorithm, particularly in its Overlap configuration corrected for bias, may be preferred over the US to calculate conditional ionisation cluster size distributions, especially when there are constraints on the simulation execution time. Finally, we found significant differences in the ionisation cluster size distributions and mean cluster sizes between the sampling algorithms and the DBSCAN clustering algorithm, with the latter resulting in several-fold higher values. The larger clusters, both in size and dimension, result from the absence of geometrical constraints beyond the input distance Eps . Additional geometrical restrictions for DBSCAN will be addressed in future work.

Acknowledgements

João F. Canhoto acknowledges financial support from Fundação para a Ciência e a Tecnologia (FCT) through the research grant PRT/BD/151544/2021.

References

- Agostinelli, S. *et al.* (2003) ‘Geant4—a simulation toolkit’, *Nuclear Instruments and Methods in Physics Research Section A: Accelerators, Spectrometers, Detectors and Associated Equipment*, 506(3), pp. 250–303. Available at: [https://doi.org/10.1016/S0168-9002\(03\)01368-8](https://doi.org/10.1016/S0168-9002(03)01368-8).
- Alexander, F. *et al.* (2015) ‘Local weighting of nanometric track structure properties in macroscopic voxel geometries for particle beam treatment planning’, *Physics in Medicine & Biology*, 60(23), p. 9145. Available at: <https://doi.org/10.1088/0031-9155/60/23/9145>.
- Allison, J. *et al.* (2006) ‘Geant4 developments and applications’, *IEEE Transactions on Nuclear Science*, 53(1), pp. 270–278. Available at: <https://doi.org/10.1109/TNS.2006.869826>.
- Allison, J. *et al.* (2016) ‘Recent developments in Geant4’, *Nuclear Instruments and Methods in Physics Research Section A: Accelerators, Spectrometers, Detectors and Associated Equipment*, 835, pp. 186–225. Available at: <https://doi.org/10.1016/j.nima.2016.06.125>.
- Baró, J. *et al.* (1995) ‘PENELOPE: An algorithm for Monte Carlo simulation of the penetration and energy loss of electrons and positrons in matter’, *Nuclear Instruments and Methods in Physics Research Section B: Beam Interactions with Materials and Atoms*, 100(1), pp. 31–46. Available at: [https://doi.org/10.1016/0168-583X\(95\)00349-5](https://doi.org/10.1016/0168-583X(95)00349-5).
- Bashkirov, V. *et al.* (2009) ‘Experimental Validation of Track Structure Models’, *IEEE Transactions on Nuclear Science*, 56(5), pp. 2859–2863. Available at: <https://doi.org/10.1109/TNS.2009.2029574>.
- Bernal, M.A. *et al.* (2015) ‘Track structure modeling in liquid water: A review of the Geant4-DNA very low energy extension of the Geant4 Monte Carlo simulation toolkit’, *Physica Medica*, 31(8), pp. 861–874. Available at: <https://doi.org/10.1016/j.ejmp.2015.10.087>.
- Bueno, M. *et al.* (2015) ‘Influence of the geometrical detail in the description of DNA and the scoring method of ionization clustering on nanodosimetric parameters of track structure: a Monte Carlo study using Geant4-DNA’, *Physics in Medicine and Biology*, 60(21), pp. 8583–8599. Available at: <https://doi.org/10.1088/0031-9155/60/21/8583>.
- Bueno, Marta *et al.* (2015) ‘PO-0824: Influence of the biological target volume modeling on ionization cluster-size distributions using Geant4-DNA’, *Radiotherapy and Oncology*, 115, pp. S415–S416. Available at: [https://doi.org/10.1016/S0167-8140\(15\)40816-3](https://doi.org/10.1016/S0167-8140(15)40816-3).

- Conte, V. *et al.* (2018) 'NANODOSIMETRY: TOWARDS A NEW CONCEPT OF RADIATION QUALITY', *Radiation Protection Dosimetry*, 180(1–4), pp. 150–156. Available at: <https://doi.org/10.1093/rpd/ncx175>.
- Conte, V., Bianchi, A. and Selva, A. (2023) 'Track Structure of Light Ions: The Link to Radiobiology', *International Journal of Molecular Sciences*, 24(6). Available at: <https://doi.org/10.3390/ijms24065826>.
- Dingfelder, M. (2012) 'Track-structure simulations for charged particles', *Health Physics*, 103(5), pp. 590–595. Available at: <https://doi.org/10.1097/HP.0b013e3182621292>.
- Dos Santos, M. *et al.* (2013) 'Influence of the DNA density on the number of clustered damages created by protons of different energies', *Nuclear Instruments and Methods in Physics Research Section B: Beam Interactions with Materials and Atoms*, 298, pp. 47–54. Available at: <https://doi.org/10.1016/j.nimb.2013.01.009>.
- Ester, M. *et al.* (1996) 'A density-based algorithm for discovering clusters in large spatial databases with noise', in *Proceedings of the Second International Conference on Knowledge Discovery and Data Mining*. Portland, Oregon: AAAI Press (KDD'96), pp. 226–231.
- Famulari, G., Pater, P. and Enger, S.A. (2017) 'Microdosimetry calculations for monoenergetic electrons using Geant4-DNA combined with a weighted track sampling algorithm', *Physics in Medicine & Biology*, 62(13), p. 5495. Available at: <https://doi.org/10.1088/1361-6560/aa71f6>.
- Francis, Z., Villagrasa, C. and Clairand, I. (2011) 'Simulation of DNA damage clustering after proton irradiation using an adapted DBSCAN algorithm', *Computer Methods and Programs in Biomedicine*, 101(3), pp. 265–270. Available at: <https://doi.org/10.1016/j.cmpb.2010.12.012>.
- Garty, G. *et al.* (2002) 'The performance of a novel ion-counting nanodosimeter', *Nuclear Instruments and Methods in Physics Research Section A: Accelerators, Spectrometers, Detectors and Associated Equipment*, 492(1), pp. 212–235. Available at: [https://doi.org/10.1016/S0168-9002\(02\)01278-0](https://doi.org/10.1016/S0168-9002(02)01278-0).
- Garty, G. *et al.* (2010) 'A nanodosimetric model of radiation-induced clustered DNA damage yields', *Physics in Medicine & Biology*, 55(3), p. 761. Available at: <https://doi.org/10.1088/0031-9155/55/3/015>.
- Grosswendt, B. (2005) 'Nanodosimetry, from radiation physics to radiation biology', *Radiation Protection Dosimetry*, 115(1–4), pp. 1–9. Available at: <https://doi.org/10.1093/rpd/nci152>.
- Grosswendt, B. and Waibel, E. (1978) 'Transport of low energy electrons in nitrogen and air', *Nuclear Instruments and Methods*, 155(1), pp. 145–156. Available at: [https://doi.org/10.1016/0029-554X\(78\)90198-2](https://doi.org/10.1016/0029-554X(78)90198-2).
- Harrison, R.L. (2010) 'Introduction To Monte Carlo Simulation', *AIP conference proceedings*, 1204, pp. 17–21. Available at: <https://doi.org/10.1063/1.3295638>.
- Incerti, S., Ivanchenko, A., *et al.* (2010) 'Comparison of GEANT4 very low energy cross section models with experimental data in water', *Medical Physics*, 37(9), pp. 4692–4708. Available at: <https://doi.org/10.1118/1.3476457>.
- Incerti, S., Baldacchino, G., *et al.* (2010) 'The geant4-dna project', *International Journal of Modeling, Simulation, and Scientific Computing*, 01(02), pp. 157–178. Available at: <https://doi.org/10.1142/S1793962310000122>.
- Incerti, S. *et al.* (2016) 'Review of Geant4-DNA applications for micro and nanoscale simulations', *Physica Medica*, 32(10), pp. 1187–1200. Available at: <https://doi.org/10.1016/j.ejmp.2016.09.007>.
- Incerti, S. *et al.* (2018) 'Geant4-DNA example applications for track structure simulations in liquid water: A report from the Geant4-DNA Project', *Medical Physics*, 45(8), pp. e722–e739. Available at: <https://doi.org/10.1002/mp.13048>.

Kawrakow, I. *et al.* (2000) 'EGSnrc: software for Monte Carlo simulation of ionizing radiation'. Available at: <https://doi.org/doi:10.4224/40001303>.

Kellerer, A.M. (1985) 'The dosimetry of ionizing radiation', *Fundamentals of Microdosimetry* [Preprint].

Lazarakis, P. *et al.* (2012) 'Comparison of nanodosimetric parameters of track structure calculated by the Monte Carlo codes Geant4-DNA and PTra', *Physics in Medicine & Biology*, 57(5), p. 1231. Available at: <https://doi.org/10.1088/0031-9155/57/5/1231>.

Lea, D.E. (1946) *Actions of radiations on living cells*. Cambridge University Press.

Meylan, S. *et al.* (2017) 'Simulation of early DNA damage after the irradiation of a fibroblast cell nucleus using Geant4-DNA', *Scientific Reports*, 7(1), p. 11923. Available at: <https://doi.org/10.1038/s41598-017-11851-4>.

Naqa, I.E., Pater, P. and Seuntjens, J. (2012) 'Monte Carlo role in radiobiological modelling of radiotherapy outcomes', *Physics in Medicine & Biology*, 57(11), p. R75. Available at: <https://doi.org/10.1088/0031-9155/57/11/R75>.

Nikjoo, H. *et al.* (1998) 'Track structure in radiation biology: theory and applications', *International Journal of Radiation Biology*, 73(4), pp. 355–364. Available at: <https://doi.org/10.1080/095530098142176>.

Nikjoo, H. *et al.* (2006) 'Track-structure codes in radiation research', *Radiation Measurements*, 41(9), pp. 1052–1074. Available at: <https://doi.org/10.1016/j.radmeas.2006.02.001>.

Palmans, H. *et al.* (2015) 'Future development of biologically relevant dosimetry', *The British Journal of Radiology*, 88(1045), p. 20140392. Available at: <https://doi.org/10.1259/bjr.20140392>.

Pszona, S., Bantsar, A. and Nikjoo, H. (2006) 'Ionization cluster size distribution for alpha particles: experiment, modelling', *Radiation Protection Dosimetry*, 122(1–4), pp. 28–31. Available at: <https://doi.org/10.1093/rpd/ncl421>.

R Core Team (2023) 'R: A Language and Environment for Statistical Computing'. R Foundation for Statistical Computing. Available at: <https://www.R-project.org/>.

Rabus, H. *et al.* (2014) 'Biologically Weighted Quantities in Radiotherapy: an EMRP Joint Research Project', *EPJ Web of Conferences*. Edited by J.-R. Filtz *et al.*, 77, p. 00021. Available at: <https://doi.org/10.1051/epjconf/20147700021>.

Ramos-Méndez, J. *et al.* (2018) 'Fast calculation of nanodosimetric quantities in treatment planning of proton and ion therapy', *Physics in Medicine & Biology*, 63(23), p. 235015. Available at: <https://doi.org/10.1088/1361-6560/aaeeee>.

Rossi, B.H.H. and Zaider, M. (1996) *Microdosimetry and its Applications*. Springer.

Rucinski, A., Biernacka, A. and Schulte, R. (2021) 'Applications of nanodosimetry in particle therapy planning and beyond', *Physics in Medicine & Biology*, 66(24), p. 24TR01. Available at: <https://doi.org/10.1088/1361-6560/ac35f1>.

Schulte, R. *et al.* (2006) 'Mapping the sensitive volume of an ion-counting nanodosimeter', *Journal of Instrumentation*, 1(04), p. P04004. Available at: <https://doi.org/10.1088/1748-0221/1/04/P04004>.

Tang, Nicolas *et al.* (2019) 'Assessment of Radio-Induced Damage in Endothelial Cells Irradiated with 40 kVp, 220 kVp, and 4 MV X-rays by Means of Micro and Nanodosimetric Calculations', *International Journal of Molecular Sciences*, 20(24), p. 6204. Available at: <https://doi.org/10.3390/ijms20246204>.

Tang, N. *et al.* (2019) 'Influence of chromatin compaction on simulated early radiation-induced DNA damage using Geant4-DNA', *Medical Physics*, 46(3), pp. 1501–1511. Available at: <https://doi.org/10.1002/mp.13405>.

Terrissol, M. and Beaudré, A. (1990) 'Simulation of Space and Time Evolution of Radiolytic Species Induced by Electrons in Water', *Radiation Protection Dosimetry*, 31(1-4), pp. 175-177. Available at: <https://doi.org/10.1093/oxfordjournals.rpd.a080660>.

Uehara, S., Nikjoo, H. and Goodhead, D.T. (1993) 'Cross-sections for water vapour for the Monte Carlo electron track structure code from 10 eV to the MeV region', *Physics in Medicine & Biology*, 38(12), p. 1841. Available at: <https://doi.org/10.1088/0031-9155/38/12/010>.